

The mass-size relation of galaxy clusters

O. Contigiani,^{1,2*} Y. M. Bahé,¹ H. Hoekstra¹

¹*Leiden Observatory, Leiden University, PO Box 9506, Leiden 2300 RA, The Netherlands*

²*Lorentz Institute for Theoretical Physics, Leiden University, PO Box 9506, Leiden 2300 RA, The Netherlands*

Accepted XXX. Received YYY; in original form ZZZ

ABSTRACT

The outskirts of accreting dark matter haloes exhibit a sudden drop in density delimiting their multi-stream region. Due to the dynamics of accretion, the location of this physically motivated edge strongly correlates with the halo growth rate. Using hydrodynamical zoom-in simulations of high-mass clusters, we explore this definition in realistic simulations and find an explicit connection between this feature in the dark matter and galaxy profiles. We also show that the depth of the splashback feature correlates well with the direction of filaments and, surprisingly, the orientation of the brightest cluster galaxy. Our findings suggest that galaxy profiles and weak-lensing masses can define an observationally viable mass-size scaling relation for galaxy clusters, which can be used to extract cosmological information.

Key words: large-scale structure of Universe – galaxies: clusters: general – methods: numerical

1 INTRODUCTION

In the Λ CDM paradigm, structure in the Universe arises from the initial density perturbations of an (almost) homogeneous dark matter distribution. Due to gravitational evolution, this leads to the appearance of collapsed structures, i.e. dark matter haloes. Some of the baryonic matter, following this process, cools down and settles at the centres of the gravitational potentials where it forms galaxies.

This mechanism has been studied through models of so-called spherical collapse (Gunn & Gott 1972; Bertschinger 1985), whose main prediction is the existence of a radius within which the material orbiting the halo is completely virialized. In general, this virial radius depends on cosmology and redshift, but both in numerical simulations and observations, fixed overdensity radii are widely used as proxies for this quantity. An example of this is r_{200m} , defined as the radius within which the average density is 200 times the average matter density of the Universe, ρ_m . The corresponding enclosed mass is known as M_{200m} .

Halo mass functions constructed with these idealized definitions can capture the effects of cosmology (Press & Schechter 1974), the nature of dark matter (Angulo et al. 2013), and dark energy (Mead et al. 2016) on the growth of structure. In the real Universe, however, this picture is complicated by the triaxiality of haloes (Dubinski & Carlberg 1991; Monaco 1995) and the existence of clumpy (baryonic) substructure (Bocquet et al. 2015).

Because the process of structure formation is hierarchical, massive haloes contain subhaloes, some of which host galaxies themselves. The resulting clusters of galaxies are the focus of this work. What makes these objects particularly unique is the fact that they are not fully virialized yet. To this day, they are still accreting both ambient material and subhaloes through filamentary structures surrounding them (Bond et al. 1996). Because of their definition, however, traditional overdensity definitions of mass are not only affected by halo

growth, but also by a pseudo-evolution due to the redshift dependence of ρ_m (Diemer et al. 2013).

Diemer & Kravtsov (2014) and More et al. (2015) were the first to note that this growth process leads to the formation of a sharp feature in the density profile that separates collapsed and infalling material. This feature, therefore, defines a natural boundary of the halo. The location of this edge, i.e. the splashback radius r_{sp} , has an obvious primary dependence on halo mass, but also a secondary dependence on accretion rate. While this behaviour can be qualitatively explained using simple semi-analytical models of spherical collapse, none of the analytical models currently proposed (Adhikari et al. 2014; Shi 2016) can fully describe its dependency on mass and accretion rate (Diemer et al. 2017). Despite this, the corresponding definition of halo mass is particularly suited to define a universal mass function valid for a wide range of cosmologies (Diemer 2020a).

In this paper, we try to bridge the gap between the theoretical understanding of the splashback feature and observational results, both past and future. The outer edge of clusters has already been extensively measured through different tracers: the radial distribution of galaxies from wide surveys (More et al. 2016; Baxter et al. 2017; Chang et al. 2018), but also their velocity distribution (Tomooka et al. 2020), and in the weak-lensing signal of massive clusters (Umetsu & Diemer 2017; Chang et al. 2018; Contigiani et al. 2019b). Furthermore, forecasts have already set expectations for what will be obtainable from near-future experiments (Fong et al. 2018; Xhakaj et al. 2019). Despite the wealth of data and studies, however, not many *splashback observables* have been proposed. The only robust application of this feature found in the literature is related to the study of quenching for newly accreted galaxies (Adhikari et al. 2020).

To achieve our goal, we make use of hydrodynamical simulations of massive galaxy clusters, which we introduce in Section 2. We focus mainly on $z = 0$, but also make use of snapshots at redshifts $z = 0.474$ and $z = 1.017$. In Section 3, we start our discussion by introducing the physical interpretation of splashback and consider the connection between the galaxy and dark matter distributions. We then

* E-mail: contigiani@strw.leidenuniv.nl

continue in Section 4 and 5, where we explain how galaxy profiles and weak-lensing mass measurements can be combined to construct a mass-size relationship for galaxy clusters. Finally, we summarize our conclusions and suggest future developments in Section 6.

2 HYDRANGEA

The Hydrangea simulations are a suite of 24 zoom-in hydrodynamical simulations of massive galaxy clusters ($\log_{10} M_{200m}/M_{\odot}$ between 14 and 15.5 at redshift $z = 0$) designed to study the relationship between galaxy formation and cluster environment (Bahé et al. 2017). They are part of the Cluster-EAGLE project (Bahé et al. 2017; Barnes et al. 2017) and have been run using the EAGLE galaxy formation model (Schaye et al. 2015), which is known to reproduce galaxy observables such as colour distribution and star formation rates. To better reproduce the observed hot gas fractions in galaxy groups, the AGNdt9 variant of this model was used (Schaye et al. 2015).

The zoom-in regions stretch to between 10 and 30 Mpc from the cluster centre, roughly corresponding to $\lesssim 10r_{200m}$. For the definition of the cluster centre, in this work, we choose the minimum of the gravitational potential. We note, however, that this choice will not impact our conclusions since we will focus on locations around r_{200m} . The particle mass of $m \sim 10^6 M_{\odot}$ for baryons and $m \sim 10^7 M_{\odot}$ for dark matter allows us to resolve galaxy positions down to stellar masses $M_* \geq 10^8 M_{\odot}$ and total masses $M_{\text{sub}} \geq 10^9 M_{\odot}$, respectively.

In Figure 1 we show the log-derivative of the stacked subhalo density $n_s(r)$ at large scales. This is the result of a fit obtained using the model of Diemer & Kravtsov (2014), and we refer the reader to the aforementioned paper and Contigiani et al. (2019b) for a detailed explanation of the model and its components. In this article, we employ this profile because it is particularly suited to capture the sharp feature visible around r_{200m} , which is the focus of this work. We optimally sample its 8-dimensional parameter space using an ensemble sampler (Foreman-Mackey et al. 2013).

In the same plot, we also include the stacked subhalo profile of the accompanying dark matter only (DMO) simulations, initialized with matching initial conditions. The two profiles match almost exactly, suggesting that baryonic effects do not alter this feature to a significant extent (see also O’Neil et al. 2020). While not shown, we report that the same conclusion can be reached by looking at the full matter distribution $\rho(r)$ in the two sets of simulations. Similarly, this feature is also visible in the number density of galaxies, $n_g(r)$.

For reference, we present a full list of the simulated clusters used in this paper and their relevant properties, some of them defined in the following sections, in Table 1.

3 SPLASHBACK

3.1 Definition

For haloes that continuously amass matter, material close to its first apocentre piles up next to the edge of the multi-stream region, where collapsed and infalling material meets (Adhikari et al. 2014). A sudden drop in density, i.e. the feature visible in the profiles of Figure 1, is associated with this process.

This intuitive picture leads to three characterizations of the splashback radius, depending on the approach used to measure or model it:

- (i) The location of the outermost phase-space caustic.

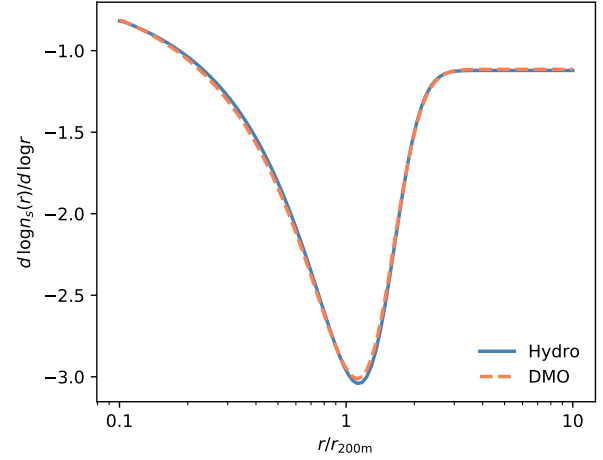


Figure 1. The splashback feature visible in the average subhalo distribution of simulated high-mass clusters. We extract the logarithmic slope by fitting a smooth profile to the mean of the Hydrangea profiles rescaled by r_{200m} . We perform this operation both on the hydrodynamical simulations (Hydro) and their dark matter only counterparts (DMO). The minimum around r_{200m} marks the halo boundary, and this figure highlights the lack of baryonic effects on the location or depth of this feature. The two logarithmic slope profiles are consistent with each other at the 1 per cent level.

- (ii) The point of steepest slope in the density profile.
- (iii) The apocentre of recently accreted material.

While these definitions have all been previously hinted at in the introduction, in this section we explicitly present them and discuss the connections existing between them. This also justifies our adopted definition, based on the density profile.

The first definition is clearly motivated in the spherical case but fails once it is applied to realistic haloes. The presence of angular momentum and tidal streams from disrupted subhaloes (see, e.g., Vogelsberger & White 2011), smooth out this feature and make its description murky. The second definition was the first suggested in the literature. Introduced by Diemer & Kravtsov (2014), it is based on the study of dark matter profiles in N-body simulations and has been linked to the first, more dynamical, definition (Adhikari et al. 2014; Shi 2016). The third was first suggested by Diemer (2017), who showed that this location can be calibrated to the second one (Diemer et al. 2017) by choosing specific percentiles of the apocentre distribution.

To clarify the relationship between the outermost caustic and apocentre, it is educational to use a self-similar toy model based on Adhikari et al. (2014) to show the phase-space distribution of a constantly accreting halo with an NFW-like mass profile (Navarro et al. 1997).

In the absence of dark energy, we follow the radial motion of particles,

$$\ddot{r} = -\frac{GM(< r, t)}{r^2}, \quad (1)$$

between their first and second turnaround in the mass profile:

$$M(r, t) = M(R, t) \frac{f_{\text{NFW}}(r/r_s)}{f_{\text{NFW}}(R/r_s)}. \quad (2)$$

We impose that the total mass evolves as $M(R, t) \propto t^{2\Gamma/3}$, $R \propto t^{2(1+\Gamma/3)/3}$, and the dimensionless NFW profile is defined as: $f(x) = \log(1+x) - x/(1+x)$. In this set of equations, Γ is the dimensionless

Table 1. The Hydrangea clusters used in this paper and their $z = 0$ properties. $\Gamma_{0.3}$ is the accretion rate measured between $z = 0$ and $z = 0.297$. The three splashback radii r_{sp} , r_{sp}^{g} , $r_{\text{sp}}^{\text{sub}}$ refer to the splashback radius measured, respectively, in the galaxy, subhalo, and dark matter distributions (see Section 3). For two clusters, CE-28 and CE-18, the radius r_{sp} is not used in this work because the dark matter distribution displays a featureless profile at large scales. All quantities are in physical units.

Name	$\Gamma_{0.3}$	$M_{200\text{m}}$ [$10^{14} M_{\odot}$]	$r_{200\text{m}}$ [Mpc]	r_{sp} [Mpc]	r_{sp}^{g} [Mpc]	$r_{\text{sp}}^{\text{sub}}$ [Mpc]
CE-0	0.8	1.74	1.74	2.98	2.72	2.60
CE-1	2.0	1.41	1.63	1.71	1.56	1.79
CE-2	0.5	1.41	1.63	2.36	3.27	2.36
CE-3	0.8	2.04	1.84	2.60	2.72	2.72
CE-4	2.8	2.19	1.89	1.63	1.87	1.79
CE-5	2.0	2.24	1.90	2.36	2.60	2.48
CE-6	1.1	3.31	2.16	2.60	2.48	2.60
CE-7	1.2	3.39	2.17	3.13	2.60	2.85
CE-8	1.8	3.09	2.12	2.26	2.48	2.06
CE-9	1.1	4.27	2.36	3.76	3.76	3.27
CE-10	0.8	3.55	2.21	3.13	3.13	2.98
CE-11	1.4	4.27	2.34	3.13	2.85	2.72
CE-12	0.1	5.13	2.49	3.43	3.76	4.13
CE-13	1.5	5.25	2.52	2.26	3.13	2.72
CE-14	2.1	6.17	2.66	2.60	2.72	2.48
CE-15	4.2	6.76	2.73	1.96	2.26	2.48
CE-16	2.7	7.59	2.84	1.42	4.13	3.43
CE-18	1.1	9.12	3.03	-	3.76	3.76
CE-21	3.7	12.30	3.34	2.36	2.85	2.60
CE-22	1.5	16.98	3.72	4.53	4.53	4.33
CE-24	1.5	15.49	3.61	3.27	3.27	4.33
CE-25	3.4	19.05	3.87	3.43	3.43	3.43
CE-28	1.9	21.88	4.06	-	3.94	3.27
CE-29	3.5	32.36	4.61	3.94	4.13	3.94

accretion rate, R represents the turnaround radius, and the scale parameter r_s is defined by the infall boundary condition

$$\frac{d \log M}{d \log r}(R) = \frac{3\Gamma}{3 + \Gamma}. \quad (3)$$

This condition, combined with the turnaround dynamics, imposes that $M(R, t) \propto (1 + z)^{-\Gamma}$.

We point out that the dependence on the time-sensitive turnaround properties $M(R, t), R(t)$ can be factored out from the equations above, meaning that the entire phase-space at all times can be obtained with a single numerical integration.

In Figure 2 we show the result of this calculation, denoting the location of the outermost caustic as r_{sp}^{c} . The caustic is formed by the outermost radius at which shells at different velocities meet ($r/r_{\text{sp}}^{\text{c}} = 1$ in the plot) and the location of shells at apocenter is defined by the intersection between the zero-velocity line and the phase-space distributions. From the figure, two things are noticeable: material at r_{sp}^{c} has not reached its apocentre yet, and the ratio between these two locations depends on the accretion rate.

It is beyond the scope of this work to quantify this dependence since it depends heavily on the mass profile inside r_{sp}^{c} . Qualitatively, however, the difference between caustic and apocentre is easy to understand once the dynamical nature of this feature is considered: the halo is growing in size, and while some material is now reaching its apocentre, mass accreted more recently has the chance to overshoot it and form the actual caustic. In a static picture, this would not be the case.

In realistic haloes, this dependence on accretion rate is only one of many factors that biases and adds scatter to the relationship between the halo boundary and apocentres. Other factors include, e.g., non-spherical orbits and the presence of multiple accretion streams.

Despite this, Diemer (2017) has shown that there is a clear link between the apocentre distribution and splashback. The percentile definition introduced there is particularly suited to theoretical investigations, but its usefulness in the very low- Γ regime is still uncertain (Mansfield et al. 2017; Xhakaj et al. 2019), and it has not been explored in the presence of modifications of gravity (Adhikari et al. 2018; Contigiani et al. 2019a).

For this work, we define the splashback radius as the location of the steepest slope as defined by a profile fit. In Table 1 we report, for each cluster, this radius measured in the distribution of galaxies, subhaloes, and total matter ($r_{\text{sp}}^{\text{g}}, r_{\text{sp}}^{\text{s}}, r_{\text{sp}}$). The model is a modified Einasto profile (Einasto 1965) with the addition of a power-law to take into account infalling material (Diemer & Kravtsov 2014). Regarding the goodness of fit, we find that up to and around $r_{200\text{m}}$ the standard deviation of the residuals is of order 10 per cent. On the other hand, the presence of substructure superimposed on a shallow density profile results in normalized residuals of order 50 per cent in the outer regions.

To further justify our approach, we show in Figure 3 how this simple definition of splashback radius is able to capture the phase-space boundary of different haloes, even when a sudden drop in density is absent. The main benefit of this definition is that it avoids the arbitrariness of the apocentre definition, or the bias induced by multiple caustics in the minimum slope definition (Mansfield et al. 2017). Its main caveats, however, are that 1) it is computationally expensive since it requires high-resolution simulations and a multi-parameter fit procedure, and 2) it might not apply to low-mass clusters and galaxy groups. We leave this last question open for future investigations.

We wrap this subsection up by stressing that this definition of “the” splashback radius is, like any other, useful only to study its

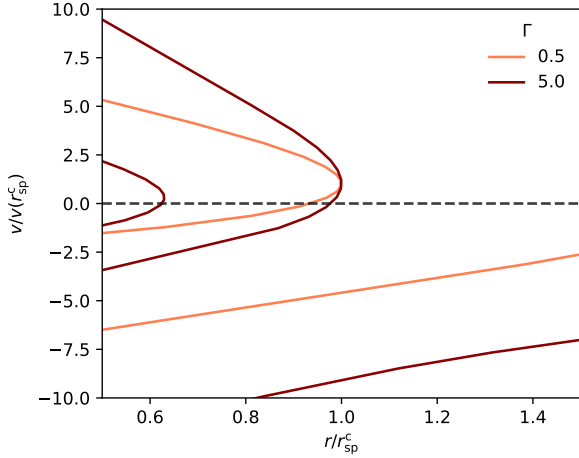


Figure 2. The phase-space structure of accreting dark matter haloes depends on the accretion rate Γ . We employ a toy model of spherical collapse to describe the multi-stream region of NFW-like haloes. For ease of readability, we have rescaled the coordinates by the location of the outermost caustic r_{sp}^c , and the velocity of collapsed material at this point. The figure shows that the material at r_{sp}^c is not necessarily at apocentre ($v = 0$) and that the ratio of these two radii is as a function of accretion rate.

correlation with other properties, or quantify the impact of different physical processes. While the flexibility of the chosen model is not surprising given the number of free parameters, the clear connection between the phase-space and the log-derivative in individual haloes is a powerful and seemingly general result. Ultimately, however, the observational results focus on stacked projected density profiles, and so should the predictions.

3.2 Accretion

It is well established (Diemer & Kravtsov 2014; More et al. 2015; Mansfield et al. 2017; Diemer 2020b) that the location of the halo boundary correlates with the accretion rate

$$\Gamma_{0.3} = \frac{\Delta \log M_{200\text{m}}}{\Delta \log(1+z)}. \quad (4)$$

In this work, this ratio is calculated in the redshift range $z = 0$ to $z = 0.293$, since this time interval roughly corresponds to one crossing time for all clusters considered here, i.e. how long ago the material currently at splashback has been accreted (Diemer 2017). Although this choice is partially arbitrary, we have investigated the dependence of our results on the redshift upper limit and we have verified that our main conclusions are not affected.

The archetypical relation demonstrating this idea is plotted in Figure 4, where we have also included the relations found in More et al. (2015), Diemer et al. (2017), and Diemer (2020b), to provide additional context. We find good agreement, even though a perfect match is not necessarily expected. The Hydrangea clusters represent a biased sample, selected to be mostly isolated at low redshift (Bahé et al. 2017). While the effect of this selection on the accretion rate distribution is not known, we show below that a connection between cluster environment and this quantity exists, and the presence of mergers might therefore influence it.

We show this relationship explicitly in Figure 5 by using one of the parameters of the profile model. As visible in the figure, the power-law index of material (both subhaloes and galaxies) outside

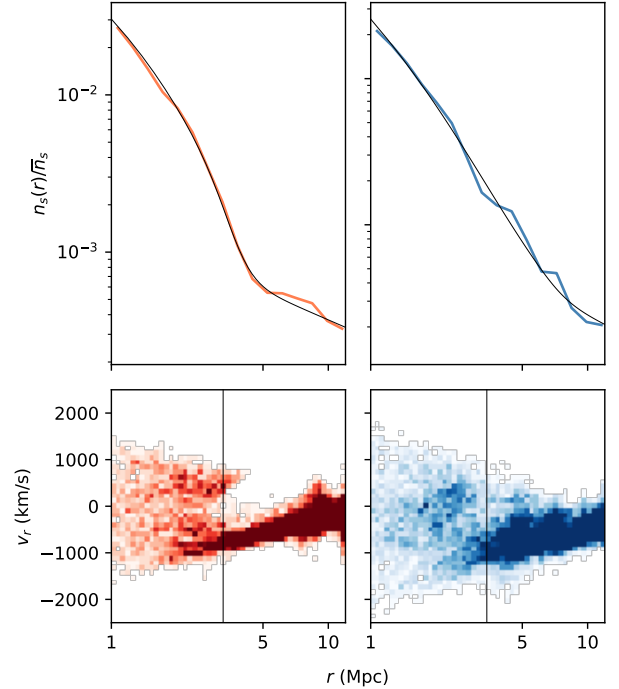


Figure 3. Fitting simulated subhalo profiles with a smooth model. In the top panels, we show the radial subhalo distributions of two clusters (CE-16, left and CE-9, right), together with the best-fit profiles used to reconstruct the log-derivative. In the bottom panels, we show how the inferred location of the log-derivative minimum (vertical line) identifies the phase-space edge of relaxed (left) and perturbed (right) galaxy clusters. In the phase-space plots, the cluster on the left is formed by collapsed particles, while the stream visible on the lower right is infalling material. The right panels demonstrate how our approach is effective even in the presence of an on-going merger when the splashback feature is not visible as a sharp transition in the density profile.

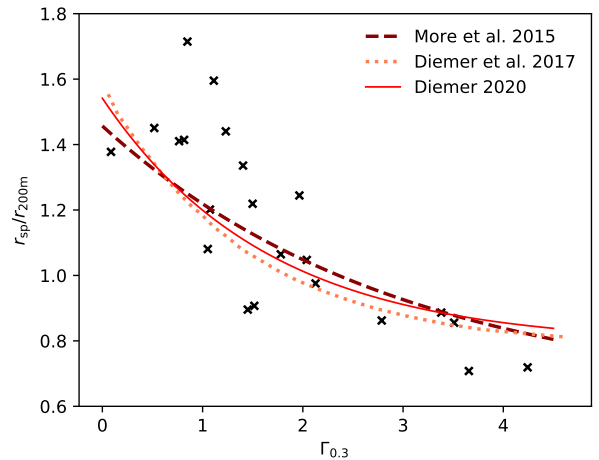


Figure 4. The splashback radius and its correlation with the accretion rate. The ratio between the splashback radius and the 200m overdensity radius correlates with the accretion rate. We show that this correlation exists for the clusters studied in this work and compare it to the relations obtained in three other studies (see text for references).

of splashback correlates with the accretion rate. To try and explain this behaviour, we use a fully consistent model of spherical collapse introduced by [Bertschinger \(1985\)](#), which was also used in [Contigiani et al. \(2019a\)](#). The set-up of this toy model is the same as what is shown in Equation (1), but with a mass profile that also needs to be solved for. Starting from an initial guess for $M(r, t) = \mathcal{M}(r/R(t))$, orbits are integrated and their mass distribution is calculated. Iterating this process multiple times returns a self-similar density profile and orbits consistent with each other.

The result of this calculation is also shown in Figure 5. Because the mass-profile prediction is not a power law, we plot a filled line displaying the range of logarithmic slopes allowed between r_{sp}^c and $2r_{\text{sp}}^c$. The fact that this prediction is not a function of accretion rate implies that the correlation between the slope and the accretion rate seen in the simulations is not purely dynamical, and suggests a connection between the cluster environment and accretion rate.

We stress here that previous splashback works have mostly focused on stacked halo profiles, for which the expectation of the spherically symmetric calculation shown above is roughly verified, even in the presence of dark energy ([Shi 2016](#)). We also recover this result for our sample (see the star symbol in Figure 5), but we point out that this is a simple conclusion. Because Newtonian gravity is additive, stacking enough clusters should always recover the spherically symmetric result. Despite this, we also note that results from the literature do not always agree with this prediction. However, we do not linger on these discrepancies since 1) this was never the focus of previous articles, and 2) different methods to extract the power-law have been employed.

This departure from the spherical case implies that anisotropies play a role in shaping the accretion rate Γ . To study the impact of accretion flows on the cluster boundary, we study 72 sky projections of the Hydrangea clusters (3 each, perpendicular to the x , y , and z axes of the simulation boxes) and rotate them to align the preferred accretion axes in these planes. For each projection, we define this direction $\theta \in (-\pi/2, \pi/2)$ in two ways: 1) to capture the filamentary structure around the cluster between $r_{200\text{m}}$ and $5r_{200\text{m}}$, we divide the subhalo distribution in 20 azimuthal bins and mark the direction of the most populated one, and 2) to capture the major axis of the BCG, we use unweighted quadrupole moments of the central galaxy’s stellar profile within 10 kpc from its centre. The mean projected distributions according to these two methods are presented in the left and right top panels of Figure 6, respectively.

Looking at the figure, it not surprising that, in the left case, filamentary structures of the cosmic web are visible around the central cluster – this is by construction. Along accretion directions, the subhalo distribution is expected to exhibit a sharper feature. As visible in the lower panel of Figure 6, the inferred 3-dimensional logarithmic derivative of the profile along filaments exhibits exactly these traits. More surprisingly, however, is the fact that these same traits are also noticeable in the mean distributions aligned according to the central galaxy’s axis.

This result implies that the distribution of stellar mass within the central 10 kpc of the cluster contains information about the distribution of matter at radii which are a factor 10^2 larger. In fact, the connection between the shape of the dark matter halo and the ellipticity of the brightest cluster galaxy (BCG, which is also the central galaxy for massive galaxy clusters) is known ([Okumura et al. 2009](#); [Herbonnet et al. 2019](#)). And, similarly to other results ([Conroy et al. 2007](#); [De Lucia & Blaizot 2007](#)), the Hydrangea simulations predict that the stellar-mass buildup of the BCG is driven by the stripping of a few massive satellites after their first few pericentre passages ([Bahé et al., in prep.](#)). Because these galaxies quickly sink to the centre,

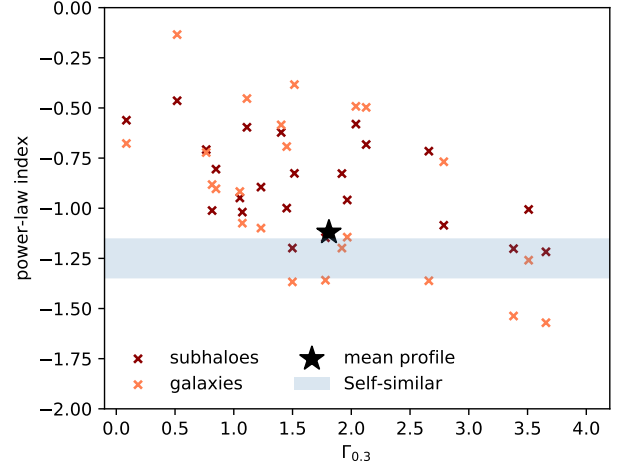


Figure 5. The distribution of subhaloes and galaxies outside the cluster edge as a function of accretion rate. Faster growing haloes display a more concentrated distribution of satellites outside of their boundary. This behaviour seen in individual clusters is not explained by simple models of spherical collapse (blue shaded area), but the average profile (marked by a star) matches the expectation. This suggests that non-isotropic processes shape this relation.

the material they leave behind is, therefore, a tracer of their infalling direction.

4 THE MASS-SIZE RELATION

In our sample, we find that the splashback feature seen in the galaxy, subhalo, and total matter profiles are all at the same location. The mean fractional difference between any two of r_{sp}^g , r_{sp}^s , or r_{sp} is consistent with zero, with a mean standard deviation of 3 per cent. We also verified that this statement is unaffected by cuts in subhalo mass or galaxy stellar mass, but we emphasize that this does not mean that galaxy selection effects have no impact on these quantities. For example, it is an established result, both in the Hydrangea simulations ([Oman et al. 2020](#)) and in observations ([Adhikari et al. 2020](#)), that the location of a galaxy in projected phase-space correlates with its colour and star-formation rate. This is because a red colour preferentially selects quenched galaxies that have been orbiting the halo for a longer time.

Until their first apocentre after turnaround, galaxies act as test particles orbiting the overdensity as the halo grows in mass. In the standard cold dark matter paradigm, based on a non-interacting particle, it is not surprising then that the edge formed in their distribution is identical to the one seen in the dark matter profile. It should be noted, however, that this is not necessarily true in extended models in which dark matter does not act as a collisionless fluid. Due to their infalling trajectories, the distribution of galaxies will always display a splashback feature, even if the dark matter profile does not exhibit one.

In the cold dark matter scenario, our result implies that galaxies can be used to trace the edge of clusters. We note, in particular, that this measurement has already been performed several times using photometric surveys ([Baxter et al. 2017](#); [Nishizawa et al. 2017](#); [Chang et al. 2018](#); [Zürcher & More 2019](#); [Shin et al. 2019](#)). Furthermore, due to the large number of objects detected, galaxy distributions obtained through this method offer the most precise measurements of splashback. The accuracy of the results, however, depends heavily

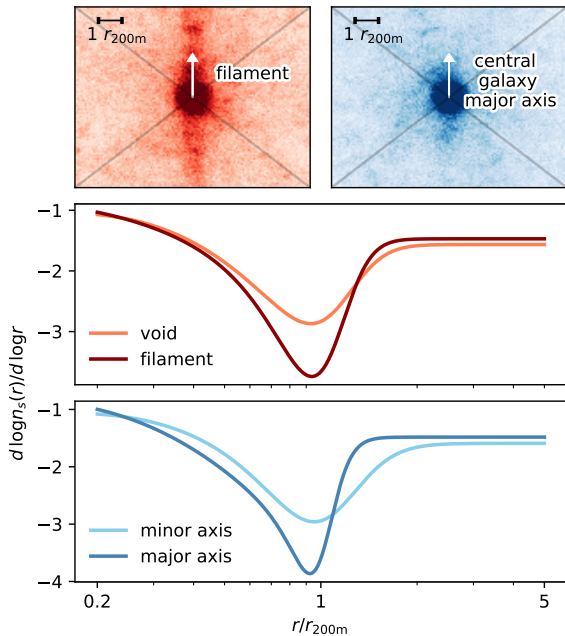


Figure 6. The impact of filaments and accretion flows on the cluster’s edge. We rotate the 2D subhalo distributions of different clusters to align their accretion axes. The top panels show the resulting mean distributions in a square region of size $5r_{200m}$ obtained with two definitions of this direction: one based on the presence of filaments outside r_{200m} (left), and one based on the central galaxy’s major axis (right). The first one better identifies the filamentary structures around the clusters, but the second one is closer to what can be observed. In the bottom panels, we show how the inferred 3-dimensional logarithmic slope inside the quadrants aligned with the accretion direction (darker shade) differs from the profile outside (lighter shade). The results from the bottom panel imply that the central galaxy’s major axis traces the direction of infalling material.

on the details of the cluster finding algorithm (Busch & White 2017; Shin et al. 2019).

With this in mind, we build an observational mass-size relation between the location of this feature in the galaxy distribution (r_{sp}^g) and the mass enclosed within it (M_{sp}^g). In Figure 7 we present the correlation between the two for the Hydrangea clusters. Because the splashback radius is roughly located at r_{200m} (see Figure 4), this relationship can be understood as a generalization of the virial mass-radius relation, where we have introduced a dependence on accretion rate. Surprisingly, we find that the dependence on $\Gamma_{0.3}$ is well captured by a simple form:

$$\frac{M_{sp}^g}{r_{sp}^3} \propto (1 + \Gamma_{0.3})^\beta. \quad (5)$$

While we do not constrain β precisely, we find that $\beta = 1.5$ provides an adequate fit by reducing the total scatter from 0.25 dex to about half of this value. This choice of exponent and functional form is supported by the model of self-similar collapse used for Figure 5, where we find that a power-law $\beta = 1.45$ fits this relationship with the same precision as the exponential functions calibrated to numerical simulations shown in Figure 4. For a more extensive comparison with these predictions, we refer the reader to Section 6.

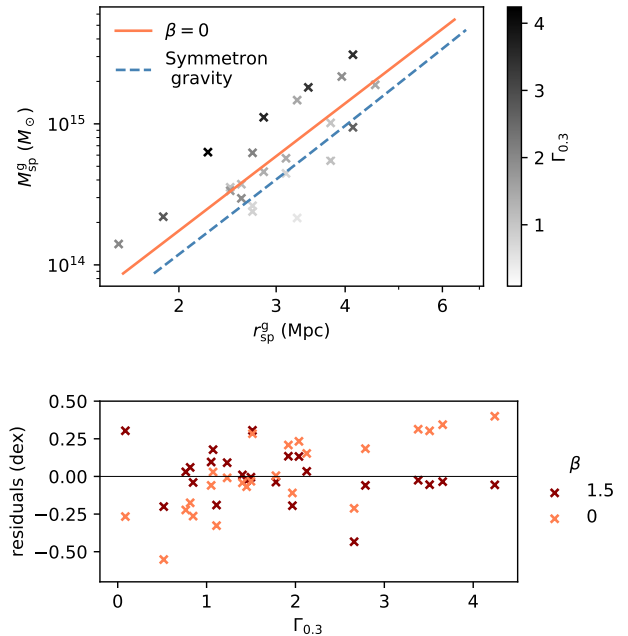


Figure 7. The mass size relation of galaxy clusters. In the top panel, we show how the size of the cluster boundary seen in the galaxy distribution, r_{sp}^g , scales with its enclosed mass, M_{sp}^g . In the same panel we also show the median relation in Equation (5) obtained for $\beta = 0$ and how modifications of gravity are expected to affect this relation (blue dashed line, see text for more details). In this relation, a secondary dependence on the accretion rate $\Gamma_{0.3}$ is a source of scatter that can be captured if $\beta \neq 0$. As visible in the residuals in the bottom panel, a simple power-law form well reproduces this dependence. In the considered sample, we find that half of the total scatter (0.25 dex) is due to the mass accretion rate distribution.

The virial relation is a trivial connection between the mass and size of haloes based on an overdensity factor, but its observational power is limited by the fact that these masses are usually extracted from parametric fits to weak-lensing profiles that do not extend to the respective overdensity radii. Because of this, the overdensity masses have a strong dependence on the assumed mass-concentration relation (see, e.g. Umetsu et al. 2020). The splashback feature, on the other hand, naturally predicts a mass-size relation for galaxy clusters and does so without the need for external calibrations.

In Figure 7 we also plot the expected change in this relation to due modifications of gravity. We use the symmetron gravity model of Contigiani et al. (2019a) with parameters $f = 1$ and $z_{ssb} = 1.5$, and assume that the change affects only the splashback radius and not the mass contained within it. The exact result depends on the theory parameters, but the expected change in this relation is around 0.15 dex.

Experimentally, we argue that this relation can be probed using a combination of galaxy density profiles (to extract r_{sp}^g) and weak lensing measurements. Aperture masses (Clowe et al. 2000), in particular, can be used to extract in a model-independent fashion the average projected mass within a large enough radius. If necessary, the aperture mass can also be deprojected to obtain a low-bias estimate (Herbonnet et al. 2020).

5 REDSHIFT EVOLUTION

So far, we have only considered the simulation predictions at $z = 0$. In this section, we extend our analysis to higher redshifts by exploring two other snapshots of the Hydrangea simulations at $z = 0.474$ and $z = 1.017$.

At these higher redshifts, we find that the scatter in the splashback relation for individual haloes is large. This is visible in Figure 8, where we plot the equivalent of Figure 4 for these two snapshots. We recover the general result of Diemer (2020b) that the average values of $r_{\text{sp}}/r_{200\text{m}}$ and Γ should be higher at early times, but the correlation between the two is completely washed out by $z = 1$. We connect this to three causes: 1) The fixed time interval between the snapshots does not allow us to reliably estimate Γ at higher redshift when the crossing times are smaller. 2) The lower number of resolved galaxies and subhaloes means that the residuals of the individual profile fits are larger around the virial radius. And finally, 3) the higher frequency of mergers at high redshift means that the numbers of haloes with profiles not displaying a clear splashback feature increases.

We find that Equation 5 is still valid, even if our ability to constrain the scatter at high redshift is impeded by the sample variance. Furthermore, we report that the splashback overdensity $M_{\text{sp}}/r_{\text{sp}}^3$ has a redshift dependence. Or, in other words, that the logarithmic zero-point that was not specified in Equation 5 is a function of redshift. Not accounting for the Γ dependence, our best fit values for the logarithm of the average overdensity $\log_{10}(M_{\text{sp}}/M_{\odot}) - 3 \log_{10}(r_{\text{sp}}/\text{Mpc})$ are $[13.3, 13.8, 14.1] \pm 0.3$ at redshifts $[0, 0.5, 1]$.

Regarding the anisotropy in the splashback feature due to filamentary structures, we report that this phenomenon exists also at high redshift. In Figure 9 we compare the sky-projected subhalo profiles $\Sigma_s(R)$ towards different directions, similarly to what we have done for Figure 6. In this case, however, we explicitly discuss the connection with observations by plotting directly the ratio of the density profiles inside quadrants oriented towards and perpendicular to the two accretion directions, instead of focusing on the result of the profile fits. The mean and variance of these ratios are calculated assuming that the different projections are independent. We find that the orientation of the major axis of the brightest cluster galaxy does not correlate with a splashback anisotropy at $z = 1$. This is because, in most cases, the identification of a central, brightest galaxy is not straightforward at this redshift. At early times, the future central galaxy is still in the process of being created from the mergers of multiple bright satellites located close to the cluster's centre of potential.

To conclude this section, we point out that in the region around $r_{200\text{m}}$, the difference between the profiles perpendicular and parallel to the central galaxy's major axis is about 10 per cent at redshift $z \lesssim 0.5$. This departure is well within the precision of galaxy profiles extracted from large surveys (e.g. Adhikari et al. 2020). Therefore, this measurement might already be possible using such catalogues.

6 DISCUSSION AND CONCLUSIONS

On its largest scales, the cosmic web of the Universe is not formed by isolated objects, but by continuously flowing matter distributed in sheets, filaments and nodes. For accreting (and hence non-virialized) collapsed structures such as galaxy clusters, the splashback radius represents a physical boundary motivated by their phase-space distributions.

Based on this idea, we have shown in this work that the full galaxy profile can be used to define a cluster mass, similarly to how richness is usually used as mass proxy (see, e.g., Simet et al. 2016). Because

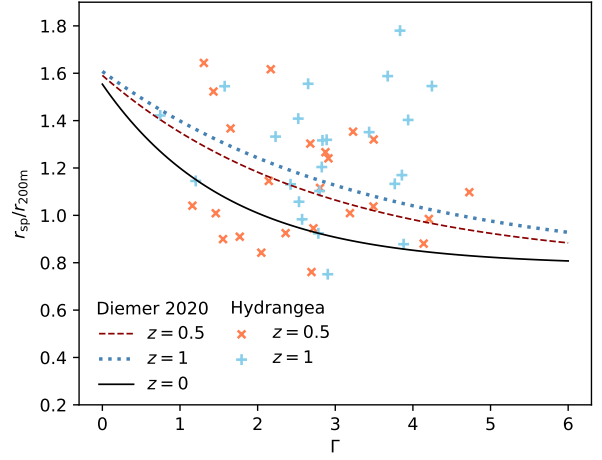


Figure 8. The splashback radius and its correlation with the accretion rate as a function of redshift. This plot is an extension of Figure 4 for redshifts $z = 0.474$ (orange crosses) and $z = 1.017$ (light blue plus symbols). The ratio between the splashback radius and the 200m overdensity radius should correlate with the accretion rate Γ , but for the Hydrangea snapshot at $z = 1.017$ the large sample variance washes out this correlation. Despite this, we still recover the expectation of previous results (plotted lines), a larger average $r_{\text{sp}}/r_{200\text{m}}$ at higher redshift.

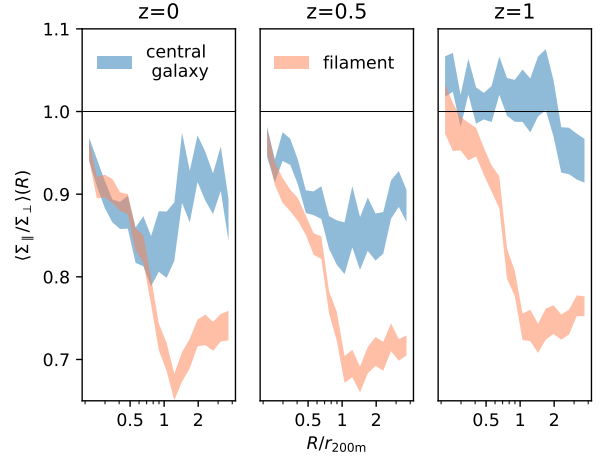


Figure 9. The impact of filaments and accretion flows on the outer density profile of massive haloes as a function of redshift. We plot the mean value and variance of the ratio between the 2D subhalo distributions in quadrants parallel (Σ_{\parallel}) and perpendicular (Σ_{\perp}) to the accretion direction defined through two tracers. This ratio is closely related to what can be measured in observations. While the difference in profile towards and away from filamentary structures is visible at all redshifts, the orientation of the central galaxy is not a good tracer of the splashback anisotropy at high redshift. This is because the central BCG is still forming and its orientation is not yet finalized.

of the dynamical nature of the equivalent feature in the dark matter profile, we conclude that, observationally, the splashback feature in the galaxy profile *defines* the physical halo mass. Moreover, we have shown here that the natural relation between the mass and size of haloes according to this definition (see Fig. 7) can be used to constrain new physics at cluster scales.

Because this boundary is delimited by recently accreted material,

we found that a majority of the scatter in this mass-size relation can be explained through a secondary dependence on accretion rate Γ . Building from this, we have also explored how this connection to the accretion rate might be interpreted as a connection between the geometry of the cosmic web and how clusters are embedded in it. The relation between the two is made explicit in Figure 5, Figure 6, and Figure 9. In these figures, we have investigated how the cluster environment affects both the halo growth and the stellar distribution of the central galaxy. This information, combined with the scatter of the mass-size relation, can therefore be used as a consistency check for any property that claims to select for accretion rate.

6.1 The role of simulations

In the last few years, the study of the splashback feature has evolved into a mature field both observationally and theoretically. We use this section to discuss explicitly the connection between the two, in light of this work and its connection to previous endeavours.

In the context of splashback, simulations have guided the creation of theoretical principles and provided expectations for observational results. Over time, as more observational results become viable, it becomes necessary to provide clear and powerful observables. Following this spirit, we used high-resolution hydrodynamical simulations to explore directly the connection between measurements based on sky-projected galaxy distributions, and theoretical predictions. In particular, we have introduced in this work two new splashback-based observables: the mass-size relation and the boundary anisotropy.

Our conclusions regarding the mass-size relation and its redshift evolution are similar to the results of Diemer et al. (2017) and Diemer (2020b), which are based on more extensive N-body simulations. For the sake of completeness, it is important to note that, in the same papers, it was also found that the splashback overdensity is not universal, but has both a mild dependency on M_{200m} and a strong dependency on cosmology, especially at low redshift ($z \approx 0.2$). Due to our limited sample, we are clearly unable to model these effects in this work. Nonetheless, we point out that our goal here is to construct a pure splashback scaling-relation based on galaxy profiles and weak lensing mass measurements. Every other dependency, if present, should be captured either as additional scatter or through different parameter values.

It is important to note that these previous works are based on the apocentre definition of splashback (see Section 3). In contrast, we defined the splashback radius as the point of steepest slope according to a model fit to the density profiles of galaxy clusters. While we do not necessarily expect the two definitions to differ, our choice is based on its connection to observations, and the desire to highlight the fact that the splashback radius is not only some abstract halo property but can be defined as a characteristic of individual profiles, such as, e.g., the concentration parameter (Navarro et al. 1997).

Our choice has, of course, its drawbacks. The versatility of the fitted model is necessary to capture the variance of the individual profiles, but the resulting intrinsic scatter is large and not the best suited to study tight splashback correlations (such as Figure 4). At the same time, the large parameter space might also be seen by some as a chance to study a multitude of correlations between different model parameters. However, we resist this temptation, as inferences based on such correlations might say more about the particular model employed than provide any physical information.

A subtler difference between our method to characterize splashback and other ones present in the literature is related to the definition of spherical density profiles. Mansfield et al. (2017) and in Deason et al. (2020) found that the most successful method to achieve a clear

splashback feature for individual haloes is to measure the median profile along multiple angular directions. In light of the results of Figure 6, we argue that the distribution of splashback as a function of direction is skewed by the presence of a few dense filaments and hence the difference between a median and mean splashback can be substantial. More importantly, we report that the splashback not only has an anisotropy in depth but also in location. While not depicted in the plot, we have seen this by focusing on the filamentary direction with a tighter azimuthal bin. Therefore, we stress that future works should exercise caution when employing such methods. The use of median profiles smooths substructure by focusing on the halo boundary in the proximity of voids, but because this process is itself correlated with the halo growth rates (see Figure 5), the connection with observations is not as simple as one might expect.

6.2 Next steps

Because in this work we have focused only on high-mass objects ($M \sim 10^{14.5} M_{\odot}$), a natural future step is to investigate if the results apply also in other regimes. For example, a larger sample over a wide range of masses and redshifts is required to confirm the simple form of Equation (5) and verify if it applies to lower mass groups ($M \sim 10^{13.5} M_{\odot}$).

Exploring a wider range in mass, both in observations and simulations, can also be used to confirm a key prediction: because the median accretion rate is expected to be a function of mass and redshift (More et al. 2015), we expect the mass-size relation for an observed halo sample to not necessarily follow a simple form.

Finally, we point out that our results encourage a concentrated effort towards understanding the relationship between cluster environment and splashback. What is discussed in Figure 5, 6 and 9 suggests that the connection between accretion-flows, filaments, and cluster boundary is not a simple one. To better understand this process, it will become necessary to complement the usual *inside-out* theoretical approaches to splashback, that look at haloes to define their boundaries, with *outside-in* approaches, that connect the cosmic web to its nodes. In this context, the amount of splashback data gathered by projects such as the Kilo Degree Survey (de Jong et al. 2013), Dark Energy Survey (The Dark Energy Survey Collaboration 2005), and, in the future, LSST (LSST Science Collaboration et al. 2009) and *Euclid* (Laureijs et al. 2011) will provide a powerful probe for the study of structure formation.

ACKNOWLEDGEMENTS

We thank Benedikt Diemer for providing valuable feedback on the manuscript. OC is supported by a de Sitter Fellowship of the Netherlands Organization for Scientific Research (NWO). HH acknowledges support from the VICI grant 639.043.512 from NWO. YMB acknowledges funding from the EU Horizon 2020 research and innovation programme under Marie Skłodowska-Curie grant agreement 747645 (ClusterGal) and the NWO through VENI grant 639.041.751. The Hydrangea simulations were in part performed on the German federal maximum performance computer “HazelHen” at the maximum performance computing centre Stuttgart (HLRS), under project GCS-HYDA / ID 44067 financed through the large-scale project “Hydrangea” of the Gauss Center for Supercomputing. Further simulations were performed at the Max Planck Computing and Data Facility in Garching, Germany.

REFERENCES

- Adhikari S., Dalal N., Chamberlain R. T., 2014, *Journal of Cosmology and Astroparticle Physics*, 2014, 019–019
- Adhikari S., Sakstein J., Jain B., Dalal N., Li B., 2018, *Journal of Cosmology and Astroparticle Physics*, 2018, 033–033
- Adhikari S., et al., 2020, arXiv e-prints, p. arXiv:2008.11663
- Angulo R. E., Hahn O., Abel T., 2013, *MNRAS*, 434, 3337
- Bahé Y. M., et al., 2017, *Monthly Notices of the Royal Astronomical Society*, 470, 4186
- Barnes D. J., et al., 2017, *Monthly Notices of the Royal Astronomical Society*, 471, 1088–1106
- Baxter E., et al., 2017, *The Astrophysical Journal*, 841, 18
- Bertschinger E., 1985, *ApJS*, 58, 39
- Bocquet S., Saro A., Dolag K., Mohr J. J., 2015, *Monthly Notices of the Royal Astronomical Society*, 456, 2361–2373
- Bond J. R., Kofman L., Pogosyan D., 1996, *Nature*, 380, 603–606
- Busch P., White S. D. M., 2017, *Monthly Notices of the Royal Astronomical Society*, 470, 4767–4781
- Chang C., et al., 2018, *The Astrophysical Journal*, 864, 83
- Clowe D., Luppino G. A., Kaiser N., Gioia I. M., 2000, *ApJ*, 539, 540
- Conroy C., Wechsler R. H., Kravtsov A. V., 2007, *The Astrophysical Journal*, 668, 826–838
- Contigiani O., Vardanyan V., Silvestri A., 2019a, *Physical Review D*, 99
- Contigiani O., Hoekstra H., Bahé Y. M., 2019b, *Monthly Notices of the Royal Astronomical Society*, 485, 408–415
- De Lucia G., Blaizot J., 2007, *MNRAS*, 375, 2
- Deason A. J., et al., 2020, *MNRAS*,
- Diemer B., 2017, *The Astrophysical Journal Supplement Series*, 231, 5
- Diemer B., 2020a, Universal at last? The splashback mass function of dark matter halos (arXiv:2007.10346)
- Diemer B., 2020b, arXiv e-prints, p. arXiv:2007.09149
- Diemer B., Kravtsov A. V., 2014, *The Astrophysical Journal*, 789, 1
- Diemer B., More S., Kravtsov A. V., 2013, *ApJ*, 766, 25
- Diemer B., Mansfield P., Kravtsov A. V., More S., 2017, *The Astrophysical Journal*, 843, 140
- Dubinski J., Carlberg R. G., 1991, *ApJ*, 378, 496
- Einasto J., 1965, *Trudy Astrofizicheskogo Instituta Alma-Ata*, 5, 87
- Fong M., Bowyer R., Whitehead A., Lee B., King L., Applegate D., McCarthy I., 2018, *Monthly Notices of the Royal Astronomical Society*
- Foreman-Mackey D., Hogg D. W., Lang D., Goodman J., 2013, *Publications of the Astronomical Society of the Pacific*, 125, 306
- Gunn J. E., Gott J. R. I., 1972, *The Astrophysical Journal*, 176, 1
- Herbonnet R., von der Linden A., Allen S. W., Mantz A. B., Modumudi P., Morris R. G., Kelly P. L., 2019, *Monthly Notices of the Royal Astronomical Society*, 490, 4889–4897
- Herbonnet R., et al., 2020, *Monthly Notices of the Royal Astronomical Society*, 497, 4684–4703
- LSST Science Collaboration et al., 2009, arXiv e-prints, p. arXiv:0912.0201
- Laureijs R., et al., 2011, Euclid Definition Study Report (arXiv:1110.3193)
- Mansfield P., Kravtsov A. V., Diemer B., 2017, *The Astrophysical Journal*, 841, 34
- Mead A. J., Heymans C., Lombriser L., Peacock J. A., Steele O. I., Winther H. A., 2016, *Monthly Notices of the Royal Astronomical Society*, 459, 1468–1488
- Monaco P., 1995, *The Astrophysical Journal*, 447, 23
- More S., Diemer B., Kravtsov A. V., 2015, *The Astrophysical Journal*, 810, 36
- More S., et al., 2016, *ApJ*, 825, 39
- Navarro J. F., Frenk C. S., White S. D. M., 1997, *The Astrophysical Journal*, 490, 493–508
- Nishizawa A. J., et al., 2017, *Publications of the Astronomical Society of Japan*, 70
- O’Neil S., Barnes D. J., Vogelsberger M., Diemer B., 2020, arXiv e-prints, p. arXiv:2012.00025
- Okumura T., Jing Y. P., Li C., 2009, *The Astrophysical Journal*, 694, 214–221
- Oman K. A., Bahé Y. M., Healy J., Hess K. M., Hudson M. J., Verheijen M. A. W., 2020, A homogeneous measurement of the delay between the onsets of gas stripping and star formation quenching in satellite galaxies of groups and clusters (arXiv:2009.00667)
- Press W. H., Schechter P., 1974, *ApJ*, 187, 425
- Schaye J., et al., 2015, *Monthly Notices of the Royal Astronomical Society*, 446, 521–554
- Shi X., 2016, *Monthly Notices of the Royal Astronomical Society*, 459, 3711
- Shin T., et al., 2019, *Monthly Notices of the Royal Astronomical Society*, 487, 2900–2918
- Simet M., McClintock T., Mandelbaum R., Rozo E., Rykoff E., Sheldon E., Wechsler R. H., 2016, *Monthly Notices of the Royal Astronomical Society*, 466, 3103–3118
- The Dark Energy Survey Collaboration 2005, arXiv e-prints, pp astro-ph/0510346
- Tomooka P., Rozo E., Wagoner E. L., Aung H., Nagai D., Safonova S., 2020, Clusters Have Edges: The Projected Phase Space Structure of SDSS redMaPPer Clusters (arXiv:2003.11555)
- Umetsu K., Diemer B., 2017, *The Astrophysical Journal*, 836, 231
- Umetsu K., et al., 2020, *The Astrophysical Journal*, 890, 148
- Vogelsberger M., White S. D. M., 2011, *MNRAS*, 413, 1419
- Xhakaj E., Diemer B., Leauthaud A., Wasserman A., Huang S., Luo Y., Adhikari S., Singh S., 2019, How Accurately Can We Detect the Splashback Radius of Dark Matter Halos and its Correlation With Accretion Rate? (arXiv:1911.09295)
- Zürcher D., More S., 2019, *The Astrophysical Journal*, 874, 184
- de Jong J. T. A., Verdoes Kleijn G. A., Kuijken K. H., Valentijn E. A., 2013, *Experimental Astronomy*, 35, 25

This paper has been typeset from a $\text{\TeX}/\text{\LaTeX}$ file prepared by the author.